Interface Engineering of 2D-C_3N_4/NiFe-LDH Heterostructure for Highly Efficient Photocatalytic Hydrogen Evolution

Jia Yan,[1,†] *Xiandi Zhang,*[1,†] *Weiran Zheng,*[1] *and Lawrence Yoon Suk Lee*[1,2,*]

[1] Department of Applied Biology and Chemical Technology and State Key Laboratory of Chemical Biology and Drug Discovery, The Hong Kong Polytechnic University, Hung Hom, Kowloon, Hong Kong SAR, China.

[2] Research Institute for Smart Energy, The Hong Kong Polytechnic University, Hung Hom, Kowloon, Hong Kong SAR, China.

† These authors equally contributed to this work.

KEYWORDS: interface engineering, layered double hydroxide, carbon nitride, photocatalysis, hydrogen evolution reaction

ABSTRACT: Photocatalytic water splitting offers an economic and sustainable pathway for producing hydrogen as a zero-emission fuel, but it still suffers from low efficiencies limited by visible-light absorption capacity and charge separation kinetics. Herein, we report an interface-engineered 2D-C_3N_4/NiFe layered double hydroxide (CN/LDH) heterostructure that shows highly enhanced photocatalytic hydrogen evolution reaction (HER) rate with excellent long-term stability. The morphology and bandgap structure of NiFe-LDH are precisely regulated by employing NH_4F as a structure-directing agent, which enables a fine interfacial tuning *via* coupling with 2D-C_3N_4. The formation of type II interface in CN/LDH enlarges active surface area and promotes the charge separation efficiency, leading to an HER rate of 3,087 μmol g^{-1} h^{-1}, which is 14 times higher than that of 2D-C_3N_4. This study highlights a rational interface engineering strategy for the formation of heterostructure with a proper hole transport co-catalyst for designing effective water-splitting photocatalysts.

1. INTRODUCTION

With recent upsurge in the demand for clean and renewable energy sources, photocatalytic water splitting has attracted considerable attention as an economical and sustainable way to produce hydrogen.[1] The key to this technology lies in the use of suitable photocatalysts that are ideally composed of non-toxic and earth-abundant elements, and capable of stable and efficient solar-light-driven H_2 evolution. Graphitic carbon nitride (g-C_3N_4), a metal-free semiconductor, has aroused much interest due to its unique properties, such as low cost, non-toxicity, high thermal, mechanical, and chemical stabilities, abundant raw material supply, and good visible light response.[2] However, hampered by its small active surface area and rapid charge recombination after irradiation, the activity of g-C_3N_4 toward water splitting is yet to be improved.[3]

Bandgap engineering is a proven route for promoting photocatalytic activity.[4-7] The band gap structure of g-C_3N_4 originates from its π-conjugated system formed by the sp^2 hybridization of C and N atoms.[8] By exfoliating g-C_3N_4 to thinner forms, its band gap can be broadened by a strong quantum confinement effect, resulting in the more positive valence band (VB) and more negative conduction band (CB) edges with much-enhanced redox capability.[9] Meanwhile, the charge transport rate is improved by the shorter diffusion path for photoexcited charges along the in-plane direction.[10] The exfoliation of bulk g-C_3N_4 also increases the exposed surface area, which benefits the reactant adsorption and surface reaction. However, the relatively large band gap of thin g-C_3N_4 nanosheets prevents efficient visible-light absorption leading to the lowered photocatalytic activity.[11] Single- or few-layer two-dimensional carbon nitride (2D-C_3N_4) possesses too large band gap that are disadvantageous for efficient light absorption and thus the charge carrier generation and transfer.

Interface engineering is often engaged to overcome such drawbacks.[12, 13] This technique is to couple the band gap of 2D-C_3N_4 with another semiconductor, which enables to enhance the visible light absorption and improve the separation and transfer kinetics of photogenerated

electrons and holes. The formation of a suitable 2D-C_3N_4-based heterostructure can provide a strong driving force for an enhancement of the charge carries separation to accelerate the photocatalytic hydrogen evolution reaction (HER) kinetics. The strong electronic coupling effects at the interface of heterostructure can modulate the interaction between each component and optimize their electronic structures to boost photocatalytic performance.[14, 15] Among the various heterostructures formed by two semiconductors, the type II staggered band alignment is one of the rational configurations to realize the effective electron–hole pair separation and transfer.[14]

Non-precious metal layered double hydroxides (LDHs) are a family of highly ordered 2D layered anionic clays generally expressed with the formula of $[M^{2+}_{1-x}M^{3+}_{x}(OH)_2]^{x+}(A^{n-})_{x/n}$ yH_2O.[16] Their unique properties, such as large specific surface area, excellent ion exchange property, well-ordered layered structure, and high controllability, make them suitable co-catalyst candidates. Besides, there are numerous choices of cation composition and layer-intercalated anion, which allows flexible control over the band gap of LDHs,[17, 18] enabling a fine interfacial tuning *via* coupling with other materials. A recent report by Boppella *et al*. demonstrated that NiFe-LDH, as a co-catalyst possessing excellent hole transfer ability, is beneficial for photocatalytic HER improvement, attributing to the effects on the spatial charge separation and the photogenerated charge recombination suppression.[19] However, it still suffered from a relatively low H_2 production rate, indicating unsatisfactory photocatalytic reaction kinetics. Finer tuning of LDH co-catalyst seems to be required to elevate the electron transfer rate, and it can be achieved by controlling the synthetic routes and conditions. As a structurally adjustable material, the morphology of NiFe-LDH was reported to vary with the addition of ammonium fluoride (NH_4F).[20] However, the effect of NH_4F-induced morphological changes on the properties of NiFe-LDH is still unknown. It is thus highly desirable to investigate the structure–activity relationships of NiFe-LDH co-catalyst for the rational design

of heterostructure and synergistic effect of components for improving the transport efficiency of photogenerated charge carriers and surface reaction kinetics.

In this report, a 2D-C_3N_4/NiFe-LDH (CN/LDH) heterostructure was constructed with adjusted band gap alignment, which enabled promoting of the photocatalytic HER kinetics by taking the advantages of 2D structures and NH_4F-induced LDH morphology regulation. The band gap structure of NiFe-LDH nanosheets was precisely tuned by the morphology control, followed by coupling with 2D-C_3N_4 to construct a Type II heterostructure of staggered band gap alignment. We demonstrated a delicate control over the composition and morphology of CN/LDH composite for promoting the transport and separation of photogenerated charge carrier, thereby achieving highly enhanced HER photoactivity and durability.

2. EXPERIMENTAL SECTION

Materials. Melamine (99 %), ammonium fluoride (NH_4F, 98 %), sodium hydroxide (NaOH, 98 %), sodium carbonate (Na_2CO_3, 99.8 %), and triethanolamine (TEOA, 99 %) were purchased from Sigma Aldrich. Nickel (II) nitrate hexahydrate ($Ni(NO_3)_2 \cdot 6H_2O$, 99 %) and Iron (III) nitrate nonahydrate ($Fe(NO_3)_3 \cdot 9H_2O$, 99 %) were purchased from Acros Organics. All chemicals were used without further purification.

Synthesis of NiFe-LDH and 2D-C_3N_4/NiFe-LDH. 2D-C_3N_4 nanosheets were synthesized *via* a calcination method according to a literature procedure.[21] The as-prepared 2D-C_3N_4 (25 mg) was first dispersed in 50 mL ultrapure water by sonication for 30 min. 2D-C_3N_4/NiFe-LDH (CN/LDH) composite was prepared following a reported procedure with slight modifications.[22] Briefly, a pre-determined amount of NH_4F was added to a 100 mL solution of $Ni(NO_3)_2 \cdot 6H_2O$ (0.48 mmol), $Fe(NO_3)_3 \cdot 9H_2O$ (0.24 mmol) and 2D-C_3N_4 nanosheets under vigorous stirring. To this reaction mixture, a 60 mL aqueous solution containing NaOH (0.72 mmol) and Na_2CO_3 (1.8 mmol) was added dropwise under vigorous stirring. After stirring for 5 h, the suspension was aged at room temperature for 24 h and collected by centrifugation, followed by washing

with water and ethanol several times until the pH reached 7. The final product was obtained as a yellow powder after freeze-drying for 12 h. The amount of NH_4F added was varied from 0 to 36, 54, 72, and 90 mmol, and the corresponding products were named as CN/LDH-1, CN/LDH-2, CN/LDH-3, CN/LDH-4, and CN/LDH-5, respectively. As a comparison, pure NiFe-LDH was obtained using the same procedure without 2D-C_3N_4 and denoted as LDH-1, LDH-2, LDH-3, LDH-4, and LDH-5 according to the amount of NH_4F used.

Material Characterizations. The morphology of the as-prepared samples was analyzed using a field emission scanning electron microscope (FE-SEM, JWSM-7001F, JEOL) and a transmission electron microscope (TEM, JEM-2100F, JEOL) operated at 200 kV. Samples for TEM analysis were prepared by drop-casting the samples dispersed in ethanol onto a holey carbon-coated 400 mesh Cu TEM grid. Elemental analyses were conducted using the energy-dispersive X-ray spectroscopy (EDX) mapping equipped on the TEM system. Structural information was acquired by X-ray diffraction (XRD) on a Bruker D8 diffractometer employing Cu Kα radiation (λ = 1.5418 Å). Zeta potential was measured using a Zeta Potential Analyzer (NanoBrook 90Plus PALS, Brookhaven Instruments Corporation). Fourier-transform infrared spectra (FT-IR) were collected with a Fourier-transform spectrophotometer (Nexus 470, Thermo Electron Corporation) using a standard KBr disk. Raman spectra were collected on a Renishaw Micro-Raman spectroscopy system with 785 nm laser excitation. The Brunauer–Emmett–Teller (BET) specific surface area, pore-volume, and pore width of the samples were characterized by nitrogen (N_2) adsorption–desorption measurements using an automatic micropore and chemisorption physisorption analyzer (ASAP 2020, Micromeritics). The pore width distributions were calculated using the adsorption branches of the N_2 adsorption–desorption isotherms by the Barrett-Joyner-Halenda (BJH) method. Prior to the N_2 adsorption–desorption measurements, all samples were degassed at 100 °C. X-ray photoelectron spectroscopy (XPS) was conducted on an ESCALAB 250Xi X-ray photoelectron spectrometer (Thermo Fisher) with a monochromic Al Kα X-ray source and a pass energy of 1486.6 eV. On

the same instrument, work functions were confirmed using ultraviolet photoelectron spectroscopy (UPS) with the excitation energy of 21.22 eV. UV–vis diffuse reflectance spectra (DRS) were taken by Cary 4000 UV-vis spectrophotometer using $BaSO_4$ as reflectance standard. Photocurrents were measured on an electrochemical workstation (Interface 1000E, Gamry Instrument). The electron spin resonance (ESR) analysis was conducted on a Bruker model ESR JES-FA200 spectrometer using the spin-trapping reagent DMPO (Sigma Chemical Co.). The photoluminescence (PL) spectra were obtained on an FLS1000 fluorescence spectrophotometer (Edinburgh Instruments) with an excitation wavelength of 325 nm. Time-resolved PL (TRPL) decay curves were recorded on the same spectrophotometer with a 325 nm pulsed laser.

Electrochemical measurements. Electrochemical properties were analyzed with a three-electrode system on a CHI 700E electrochemical station using a saturated Ag/AgCl electrode and a platinum wire as the reference and counter electrode, respectively. Catalyst ink was prepared by dispersing the as-prepared product (1 mg) in a mixture of deionized water (750 μL) and isopropyl alcohol (250 μL), followed by sonication for 30 min. The ink (20 μL) was drop-cast onto an indium-tin oxide glass (ITO, 0.5 cm × 1 cm) and used as a working electrode. In photocurrent measurements and electrochemical impedance spectroscopy (EIS), 0.1 M Na_2SO_4 solution and 5 mM $[Fe(CN)_6]^{3-/4-}$ equimolar solution containing 0.1 M KCl were used as the electrolyte, respectively. Inductively coupled plasma optical emission spectrometry (ICP-OES) was performed using an inductive coupled plasma mass spectrometer (Agilent 7500ce ICP-MS).

Photocatalytic hydrogen evolution reaction. As-prepared catalyst (3 mg) was dispersed in 25 mL triethanolamine (TEOA, 10 %) aqueous solution. After degassing with Ar for 30 min, the suspended solution was irradiated with a solar simulator (Newport, 450 W solar simulator, 1 sun) equipped with an AM 1.5 air mass filter for 5 h. The reaction product in the headspace was periodically sampled with a gas-tight syringe and analyzed by an Agilent 7890 B gas chromatograph equipped with a thermal conductivity detector (TCD) using N_2 as the carrier

gas. Apparent quantum efficiency (AQE) was analyzed using a 300 W Xenon lamp (PLS-SXE 300C (BF), PerfectLight, Beijing) with a filter (λ = 385 nm, ± 10 nm).

3. RESULTS AND DISCUSSION

3.1. NH_4F-induced morphology evolution of LDH

NiFe-layered double hydroxide (NiFe-LDH) was prepared by adding a pre-determined amount of NH_4F, a structure-directing agent, to a 100 mL solution containing $Ni(NO_3)_2$ and $Fe(NO_3)_3$ under vigorous stirring. To this reaction mixture, a 60 mL aqueous solution containing NaOH and Na_2CO_3 was added dropwise under vigorous stirring. In the absence of F^-, the rapid reactions of Ni^{2+} and Fe^{3+} with OH^- and CO_3^{2-} result in a structure without fine features, which is similar to the aggregated nanoparticles (LDH-1, **Figure 1a**). With the addition of 36 mmol NH_4F, thin flakes are evident in the scanning electron microscopic (SEM) image in **Figure 1b**, which self-stack and cluster to form a three-dimensional (3D) structure of nanoflowers (average d = 200 nm, LDH-2). **Figure 1c** shows the typical morphology of LDH employing 54 mmol NH_4F (LDH-3). A transition electron microscopic (TEM) image (inset in **Figure 1c**) reveals the self-assembled 3D structure of nanoflowers (average d = 250 nm) consisting of individual petal-like thin flakes of *ca*. 15 nm thickness and uniform distributions of Ni, Fe, and O elements (**Figure 1f**). Further increasing of NH_4F slightly reduces the average diameter to 170 nm (72 mmol NH_4F, LDH-4, **Figure 1d**), and eventually the morphology of LDH-5 changes to the aggregated nanoparticles (90 mmol NH_4F, **Figure 1e**). Apparently, NH_4F plays an important role in controlling the morphology of LDH, and we speculate that it contributes to the coordination of F^- with the metal ions, as well as the pH regulation by NH_4^+. The Fe^{3+} ions precipitate rapidly upon the addition of a solution containing OH^- and CO_3^{2-} without NH_4F addition, forming $Fe(OH)_3$ that provides the subsequent nucleation sites for Ni^{2+} ions. Because of the large difference in their solubility products (K_{sp} of $Fe(OH)_3$ and $Ni(OH)_2$ are 2.79×10^{-39} M^4 and 5.48×10^{-16} M^3, respectively), the aggregated nanoparticles (LDH-1) are formed with

such a rapid (acid–base) reaction. In the presence of NH_4F, however, Ni^{2+} and Fe^{3+} ions could be fully coordinated with F^- ions to form the intermediates of $[NiF_x]^{2-x}$ and $[FeF_y]^{3-y}$, respectively,[23] and the NH_4^+ ions act as a buffer that helps to maintain the solution pH at around 6 (**Table S1**). Under such conditions, the LDH nucleation and growth rate in the subsequent reaction with OH^- and CO_3^{2-} could be slowed down, thus allowing the formation of NiFe-LDH nanosheets.[23] The nanoflower structure would be formed by self-assembly of newly generated NiFe-LDH sheets on the pre-formed layers. An excessive amount of NH_4^+, however, makes the reaction media alkaline and hinders the formation of a hydrotalcite-type LDH structure. The main reactions of metal ions in the nucleation step are given below.

$$Ni^{2+} + xF^- \rightarrow [NiF_x]^{2-x} \quad (1)$$

$$Fe^{3+} + yF^- \rightarrow [FeF_y]^{3-y} \quad (2)$$

$$[NiF_x]^{2-x} + \tfrac{(2-a)}{2}CO_3{}^{2-} + aOH^- + bH_2O \rightarrow Ni(OH)_a(CO_3)_{\frac{(2-x)}{2}} \cdot bH_2O + xF^- \quad (3)$$

$$[FeF_y]^{3-y} + \tfrac{(3-c)}{2}CO_3{}^{2-} + cOH^- + dH_2O \rightarrow Fe(OH)_c(CO_3)_{\frac{(3-y)}{2}} \cdot dH_2O + yF^- \quad (4)$$

The Ni^{2+} and Fe^{3+} species are first coordinated with F^- ions to form $[NiF_x]^{2-x}$ and $[FeF_y]^{3-y}$ intermediates, respectively (Reaction (1) and (2)). These intermediates slowly release the metal ions to the solution upon the addition of NaOH and Na_2CO_3, forming NiFe-LDH ($Ni(OH)_a(CO_3)_{[(2-x)/2]}\cdot bH_2O$ and $Fe(OH)_c(CO_3)_{[(3-y)]}\cdot dH_2O$) (Reaction (3) and (4)).[23] To further comfirm the role of NH_4F, the synthesis of LDH-3 was repeated and the NH_4F was added at the last step. SEM and TEM images (**Figure S1**) reveal its lumpy structure which is different from the 3D flower structure of LDH-3 (**Figure 1c**). This clearly demonstrates that NH_4F directs the structural evolution of LDH, rather than acting as an etchant.

3.2. Structural characterizations

The crystal structure of as-prepared LDH samples was investigated using X-ray diffraction (XRD) spectroscopy and compared in **Figure 2**. A similar XRD pattern of hydrotalcite-type NiFe-LDH structure (JCPDS#51-0463)[24] is observed from LDH-1~3 samples. The diffraction

peaks at 11.5°, 22.9°, 34.6°, 39.0°, 46.1°, 60.0°, and 61.3° are assigned to the (003), (006), (012), (015), (018), (110), and (113) planes,[24] respectively. The XRD peaks for (015) and (018) planes are missing in LDH-1, because of poor crystallinity. The peak assigned to the (113) plane intensifies in LDH-2 and LDH-3 with improved crystallinity. New peaks appear at 11.8°, 16.8°, 26.7°, 34.0°, 35.2°, 39.2°, 46.4°, 52.0°, 55.9°, 61.1°, and 64.4° in LDH-4 and become evident in LDH-5, which can be attributed to another crystal phase of akaganeite β-FeOOH (JCPDS#34-1266). Such phase transition is consistent with the SEM and TEM characterizations, suggesting that a high concentration of NH_4F causes the reaction environments (*i.e.*, pH change by NH_4^+) to change in favor of the formation of β-FeOOH. Under the reaction conditions used, the surface of β-FeOOH is positively charged (isoelectric point at pH = *ca.* 8),[25] which prevents the nucleation of Ni^{2+} ions on its surface, as evidenced by the solution color change from yellow (Fe^{3+}) to green (Ni^{2+}) due to unreacted Ni^{2+} ions (**Figure S2a**). This is also supported by energy-dispersive X-ray spectroscopy (EDX) elemental analysis and inductively coupled plasma optical emission spectrometry (ICP-OES) that show no Ni atoms in the LDH-5 (**Table S2**).

To further understand the structural evolution of NiFe-LDH, Fourier-transform infrared (FT-IR) spectroscopy was engaged to probe the chemical structures (**Figure 2b**). The bands in the low wavenumber region between 500 and 900 cm^{-1} are related to the Fe−O, Ni−O, and Ni−O−Fe vibration modes,[26] and the peak at *ca.* 1,359 cm^{-1} corresponds to the stretching vibration of CO_3^{2-} groups.[27] Those peaks gradually intensify from LDH-1 to LDH-3, which indicates that more CO_3^{2-} ions are inserted in the interlayer of NiFe-LDH. However, the intensity of the C−O peak in LDH-4 and LDH-5 diminishes, and the new peaks appear at *ca.* 847 and 697 cm^{-1}, which are attributed to the −OH bending modes in β-FeOOH.[28, 29] These phenomena indicate that NiFe-LDH changes into the phase of β-FeOOH, which agrees well with the XRD results. In addition, all LDH samples show a broad peak at *ca.* 3,432 cm^{-1} corresponding to the O−H stretching vibration of hydroxyl groups,[27] which arises from the LDH

(Ni/Fe−OH) and interlayer water molecules. The corresponding H−OH bending vibration of water molecules appears at *ca.*1,636 cm^{-1}.[30] The broad band of O−H stretching vibration obviously shifts to a low wavenumber region in LDH-4 and LDH-5, which may be caused by the formation of β-FeOOH.

The chemical bonding and surface valence states of the LDH samples were characterized by X-ray photoelectron spectroscopy (XPS). The survey XPS spectra of the as-prepared LDHs are given in **Figure S2b**, which indicate the presence of Ni, Fe, O, and C. The high-resolution Fe 2p spectra of LDHs (**Figure 2c**) exhibit peaks at *ca*. 712.5 and 726.0 eV (green) assigned to Fe $2p_{3/2}$ and $2p_{1/2}$ along with two satellite peaks (Sat*, pink), which confirms the Fe^{3+} species in NiFe-LDH.[31] High-resolution Ni 2p spectra (**Figure 2d**) can be fitted with two spin-orbit doublets of Ni $2p_{3/2}$ and $2p_{1/2}$ at *ca*. 874 and 856 eV (green) and the two corresponding shake-up satellites (Sat*, pink) that are assigned to Ni^{2+} species in NiFe-LDH.[30, 32] Besides, a new pair of peaks (purple) at *ca*. 724 and 711 eV in LDH-4 and LDH-5 is assigned to Fe^{3+} species of FeOOH.[33] A gradual phase transition from $Fe(OH)_3$ to β-FeOOH is suggested to occur in LDH-4 and LDH-5. Interestingly, the Fe 2p and Ni 2p peaks progressively shift to the higher binding energies from LDH-1 to LDH-5. Such shifts in binding energy from LDH-1 to LDH-3 can be attributed to the morphology change from anisotropic nanoparticles to orientated nanosheets and the oxidizing environments for surface Ni and Fe species due to the surface-absorbed OH radicals. The gradual phase transformation to β-FeOOH observed from LDH-4 and LDH-5 also causes the binding energy shift.

3.3. Band gap analysis

UV-vis and valence band (VB) XPS spectroscopies were engaged to investigate the band structure of NiFe-LDH samples and understand the impact of morphological and electronic structure variations on their band gap structure.[34] From the UV-vis absorption spectra shown in **Figure 3a**, the band gaps of LDH-1 to LDH-5 are estimated to be 2.01, 2.27, 2.34, 2.26, and 2.25 eV, respectively. By extrapolating the left slope of VB_{XPS} spectra to the baseline, the VB_{XPS}

is determined as 1.44, 1.91, 2.12, 1.89, and 2.81 eV for LDH-1 to LDH-5 (**Figure 3b**). Based on these values, the valence band potentials (E_{VB}) are calculated to be 1.35, 1.82, 2.03, 1.80, and 2.72 V (*vs.* RHE, pH = 7) for LDH-1 to LDH-5 using Equation (1),[35] where Φ is the electron work function of the analyzer (4.35 eV). The conduction band potentials (E_{CB}) are then calculated as −0.66, −0.45, −0.31, −0.46, and +0.47 V for LDH-1 to LDH-5. The proposed band structures of LDHs are presented in **Figure 3c**. The smallest band gap energy (E_g) is found in LDH-1 with the lowest CB and VB potentials, and the E_g gradually increases in LDH-2 and LDH-3. The LDH-4 and LDH-5 do not follow such trend of band gap structure change, which might be caused by the phase transformation and the destruction of the hydrotalcite-type structure.

$$E_{VB} = \Phi + VB_{XPS} - 4.44 \quad (1)$$

3.4. Synthesis and morphology analysis of 2D-C_3N_4/NiFe-LDH heterostructures

The morphology and band gap structure of the NiFe-LDHs were systematically regulated by employing the NH_4F as a structure-directing agent, which enables a fine interfacial tuning *via* coupling with 2D-C_3N_4. **Figure S3** shows the synthetic procedure for the heterostructure composed of 2D-C_3N_4 and NiFe-LDH (CN/LDH), which also engaged NH_4F as a structure-directing agent. With the zeta potential of −25.3 mV (**Table S3**), the surface of 2D-C_3N_4 entraps the metal ions *via* electrostatic interactions, serving as the nucleation sites for *in situ* NiFe-LDH growth. The Ni and Fe precursors yield NiFe-LDH on the surface of 2D-C_3N_4, forming a unique heterostructure by the reactions (1) – (4). The presence of NH_4F plays an important role in modulating the nucleation rate, as described in the pristine NiFe-LDH formation, and activating the substrate.[36, 37]

Figure 4 shows the SEM and TEM images of 2D-C_3N_4 and the as-prepared CN/LDH samples. The pristine 2D-C_3N_4 exhibits the characteristic thin layered structure with large lateral sizes of *ca*. 300 nm (**Figure 4a**), which provides abundant nucleation sites for anchoring the NiFe-LDH. As shown in **Figure 4b–4d**, the morphology of CN/LDH evolves from a rough-

surfaced structure to well-structured 3D flowers as the gradually increases to 54 mmol. Further increase of added NH_4F amount to 72 mmol results in a layered agglomeration (**Figure 4e**), and finally aggregated particles are formed at 90 mmol NH_4F addition (**Figure 4f**). The amount of NH_4F during the synthesis of CN/LDHs exerts a similar impact on the morphological evolution as in that of pristine LDHs (**Figure 1**).

Upon the formation of CN/LDH-3 nanoflowers, as an example, the diameter of each nanosheet has slightly increased (280 nm, **Figure 4d**) compared with that of pristine LDH-3 (250 nm, **Figure 1c**) due to the incorporation of 2D-C_3N_4. The high-resolution TEM (HRTEM) image of CH/LDH-3 (**Figure 4g**) reveals two distinct areas; one with amorphous structure and the other exhibiting lattice fringes with *d*-spacing of 0.24 nm, which correspond to 2D-C_3N_4 and the (012) plane of LDH, respectively. The EDX elemental mapping images of CN/LDH-3 display the homogeneous distribution of C, N, Ni, Fe, and O elements (**Figure 4h** and **4i**), confirming the successful construction of CN/LDH-3 heterostructure.

3.5. HER properties of CN/LDH heterostructures

It was reported that LDH could act as a hole transfer mediator in photocatalytic reactions.[19] 2D-C_3N_4 with a high-degree π-conjunction network and suitable conduction band possesses a good capability for photocatalytic H_2 evolution, but it still suffers from the accumulation of holes in the valence band.[38] Therefore, coupling LDH with 2D-C_3N_4 can potentially benefit the electron–hole separation and thereby promote photocatalytic HER activity. To verify this, the photocatalytic activities of the interface-engineered CN/LDH composites were tested for water splitting. Given the structural/morphological changes in LDH triggered by NH_4F, the photocatalytic activities of individual components (pristine LDHs and 2D-C_3N_4) were first investigated using TEOA as a hole (h^+) scavenger under simulated sunlight. The LDHs show no photocatalytic activities despite having a suitable band gap for H_2 evolution ($E_{(H+/H2)} = -0.41$ V *vs.* RHE, pH = 7, **Figure 3c**), possibly due to the rapid recombination of photogenerated electron–hole pairs. Meanwhile, 2D-C_3N_4 exhibits relatively low H_2 production rate of 225

μmol g^{-1} h^{-1}. The as-formed CN/LDH heterostructures exhibit significantly promoted photocatalytic H_2 production rates, as shown in **Figure 5a**. Under simulated sunlight, the H_2 production rates of 2D-C_3N_4, CN/LDH-1, CN/LDH-2, CN/LDH-3, CN/LDH-4, and CN/LDH-5 are calculated to be 225, 1,341, 2,420, 3,087, 2,199, and 1,403 μmol g^{-1} h^{-1}, respectively. The CN/LDH-3 records the highest HER rate that is *ca*. 14 times higher than that of 2D-C_3N_4, and shows an apparent quantum efficiency (AQE) of 8.6 % at 385 nm. Such highly improved photocatalytic activities could be ascribed to the synergistic effect of LDH and 2D-C_3N_4, which arises from the efficient charge separation at the CN/LDH interface. The HER rates of 2D-C_3N_4 and all CN/LDH composites are further boosted with the loading of 3 wt.% Pt, the most common co-catalyst to aid H_2 production.[39] The HER rates of Pt-loaded 2D-C_3N_4, CN/LDH-1, CN/LDH-2, CN/LDH-3, CN/LDH-4, and CN/LDH-5 are 1,982, 2,803, 4,593, 6,817, 4,008, and 3,017 μmol g^{-1} h^{-1}, respectively. A similar trend of HER activities as in the CN/LDH composites is observed from these Pt-loaded CN/LDH composites. The intimate interface between 2D-C_3N_4 and LDH is believed to promote H_2 production and contribute to the durability of the composite. The CN/LDH-3 shows negligible activity loss in five consecutive 5 h-runs without refreshing the hole scavenger (**Figure 5b**). The LDH-3 in the composite is believed to participate in the hole transfer process, supplementing the role of TEOA for the long-term stable catalytic reaction.[19]

3.6. Structural Characterization of CN/LDH heterostructures

To understand such interfacial effects, the structural and electronic properties of CN/LDH-3 were systematically investigated. The XRD patterns of 2D-C_3N_4, LDH-3, and CN/LDH-3 are compared in **Figure 6a**. The CN/LDH-3 exhibits all the characteristic diffraction peaks of LDH-3 with an additional peak at 27.8°, which arises from 2D-C_3N_4 (002) interlayer stacking, indicating the co-existence of 2D-C_3N_4 and LDH-3. **Figure 6b** compares the FT-IR spectra of 2D-C_3N_4, LDH-3, and CN/LDH-3 samples. The typical adsorption peaks at 807 and 891 cm^{-1} in 2D-C_3N_4 are attributed to the bending vibration mode of *s*-triazine units and stretching

vibration of the N–H bond, respectively. The multiple bands at 1,240~1,640 cm^{-1} are assigned to the stretching vibrations of aromatic C–N and C=N heterocycles. From the CN/LDH-3, the characteristic peaks of both 2D-C_3N_4 and LDH-3 are observed, and the broad band at 3,000~3,600 cm^{-1} is attributed to the N–H and O–H stretching of 2D-C_3N_4 and LDH-3, respectively,[40] confirming the composite formation. To gain further insights into the interaction between LDH-3 and 2D-C_3N_4, Raman spectra were collected (**Figure 6c**). The Raman peaks at 460 and 542 cm^{-1} are assigned to the Fe^{3+}–O–Fe^{3+} and Fe^{3+}/Ni^{2+}–O–Ni^{2+} vibrations of NiFe-LDH.[41] 2D-C_3N_4 displays Raman peaks at 472, 707, and 770 cm^{-1}, which could be assigned to the layer–layer deformation vibrations or the correlation vibrations induced by the layer–layer vibrations, while another band at 1,233 cm^{-1} can be ascribed to the C (sp^2) bending vibration.[41] The Raman spectrum of the CN/LDH-3 exhibits all the representative peaks and a strong electrostatic bonding interaction between the two components, which verifies the CN/LDH-3 heterostructure.

Figure S4a–c compares the N_2 adsorption–desorption isotherms collected from 2D-C_3N_4, LDH-3, and CN/LDH-3, where all isotherms and hysteresis loops can be ascribed to the IV-type and H_3-type, respectively, indicating the existence of slit-shaped mesopores.[32] The pore width distribution curves confirm that the mesopore is the dominant type (insets in **Figure S4**), which is advantageous for the mass transfer kinetics. The composite formation with 2D-C_3N_4 also considerably increases the surface area and mesopore volume of LDH-3. The BET specific surface area and the corresponding pore volume of CN/LDH-3 are calculated to be 173.3 m^2 g^{-1} and 3.2 cm^3 g^{-1} nm^{-1}, respectively, which are larger than those of pristine LDH-3 (127.1 m^2 g^{-1} and 2.1 cm^3 g^{-1} nm^{-1}). The BET specific surface areas of CN/LDH-1, CN/LDH-2, CN/LDH-4, and CN/LDH-5 are estimated to be 48.2, 167.4, 162.3, and 154.8 m^2 g^{-1}, respectively (**Figure S5a–d**). Similarly, the corresponding pore volumes of CN/LDH-1, CN/LDH-2, CN/LDH-4, and CN/LDH-5 are calculated to be 0.4, 1.7, 1.5, and 1.4 cm^3 g^{-1} nm^{-1} (insets in **Figure S5a–d**). Both BET specific surface area and the corresponding pore volume

of CN/LDH samples show the same volcano-type trend observed for HER properties, confirming the structure–activity relationships in CN/LDH heterostructure.

The surface oxidation state and electronic interaction between 2D-C_3N_4 and LDH were studied using XPS. **Figure 6d** shows the high-resolution N 1s XPS spectrum of 2D-C_3N_4, which is deconvoluted into four peaks. The peaks at 398.73 and 400.33 eV correspond to the hybrid nitrogen of sp^2 (C–N=C) and tertiary nitrogen (N–$(C)_3$), respectively. The weak peak at 401.42 eV indicates the presence of ammonia nitrogen (C–N–H), which originates from the incomplete condensation of poly(tri-*s*-triazine) structures. The peak at 404.35 eV is attributed to the charging effects or positive charge localization in the heterocycles.[42] From the CN/LDH-3, these four peaks are also observed at slightly higher binding energies of 398.89, 400.47, 401.57, and 404.50 eV, respectively, indicating the decreased electron density of N species. The high-resolution Fe 2p spectra of LDH-3 and CN/LDH-3 (**Figure 6e**) exhibit a set of peaks at *ca*. 712 and 726 eV (green) assigned to Fe $2p_{3/2}$ and $2p_{1/2}$ along with two satellite peaks (Sat*, pink), confirming the presence of Fe^{3+} species in NiFe-LDH.[31] Also, the high-resolution Ni 2p spectra (**Figure 6f**) can be fitted with two spin-orbit doublets of Ni $2p_{3/2}$ and $2p_{1/2}$ at 856.70 (green) and 874.40 eV (green) and two corresponding shake-up satellites (Sat*, pink), which are attributed to Ni^{2+} species in NiFe-LDH.[30] It is interesting that CN/LDH-3 displays distinct shifts to lower binding energies for the Fe 2p peaks but to higher binding energies for the N 1s peaks, implying that the electron density has increased in the Fe species. According to the electron shielding effect, such opposite shifts of N 1s and Fe 2p peaks of CN/LDH-3 suggest that the electrons are transferred from 2D-C_3N_4 to LDH-3 in CN/LDH-3 through the surface binding interaction between N and Fe species.[19]

3.7. Photocatalytic mechanism of CN/LDH heterostructures

Further effort was made to understand the photochemical properties of the composites by engaging photocurrent measurements and electrochemical impedance spectroscopy (EIS) as shown in **Figure 7a** and **7b**. For the pristine LDH-3 photoelectrode, only traces of current

density (0.02 μA) are measurable, while 2D-C_3N_4 and CN/LDH-3 show 0.18 and 0.28 μA, respectively. The formation of CN/LDH composite intensifies the photocurrent response (on/off ratio) by *ca*. 1.5 times higher than that of 2D-C_3N_4, demonstrating an enhanced surface reaction kinetics and superior electron–hole pair separation. This result is in excellent accordance with the photocatalytic performances. **Figure 7b** displays the Nyquist plots obtained from the EIS measurements at open circuit potential (OCP), together with the equivalent electrical circuit. All samples exhibit a semicircle and a straight line in the high and low-frequency regions, which correspond to the charge transfer resistance (R_{ct}) and diffusion resistance (Z_w), respectively.[43] The x-intercept of the Nyquist plot represents the non-compensated resistance (R_s) that is the sum of the resistances from electrode and electrolyte.[44] As shown in **Table S4**, the R_{ct} of CN/LDH-3 (26.76 Ω) is significantly decreased compared with both 2D-C_3N_4 (126.4 Ω) and LDH-3 (81.93 Ω), indicating a facilitated charge transport kinetics between LDH-3 and 2D-C_3N_4.[45]

Photoluminescence (PL) behavior originates from the recombination of photoinduced electron–hole pairs, which can reveal the separation and transformation of photogenerated charge carriers.[46] As shown in **Figure 7c**, the PL intensity of CN/LDH-3 decreases sharply compared with that of 2D-C_3N_4, indicating significantly suppressed radiative recombination of photogenerated charge carriers, which benefits the separation of electron–hole pairs. In addition, time-resolved PL (TRPL) spectra (**Figure 7d**) are also collected to investigate the dynamics of photogenerated charge carrier transfer, and the obtained decay curves are fitted based on the bi-exponential kinetic function equation (2):

$$I(\mathrm{t}) = A_1 \times \exp\left(-\frac{t}{\tau_1}\right) + A_2 \times \exp\left(-\frac{t}{\tau_2}\right) \qquad (2)$$

The decay times (τ_1 and τ_2) and relative amplitudes of the decay species (A_1 and A_2) are summarized in **Table S5**. The short lifetime (τ_1) reflects the radiation process attributed to the recombination of free electrons and holes, which leads to the fluorescence emission,[47] whereas

the long lifetime (τ_2) reveals the non-radiation energy transfer processes originated from the indirect formation of self-trapped excitons by the trapped electrons.[48] The τ_1 of CN/LDH-3 is measured to be longer (3.60 ns) than that of 2D-C_3N_4 (3.00 ns), which implies that the recombination rate of photoinduced electron–hole pairs over CN/LDH-3 is effectively suppressed. On the other hand, the τ_2 of 2D-C_3N_4 and CN/LDH-3 are 17.66 and 21.14 ns, respectively, revealing that CN/LDH-3 has a high probability and priority of participating in a series of photocatalytic reactions.[47] These results further demonstrate a successful construction of CN/LDH-3 heterostructure with a suitable band gap alignment that provides a strong driving force for effective separation of photogenerated electron–hole pairs as well as their efficient migration to the surface, contributing to the enhanced photocatalytic H_2 production.

To investigate the mechanism involved in the enhanced photocatalytic HER on CN/LDH-3, the absolute band positions of individual components in the heterojunction system together with the charge transfer direction need to be clarified. Diffuse reflectance UV-vis absorption studies show that the incorporation of 2D-C_3N_4 and NiFe-LDH significantly extends the absorption edge of 2D-C_3N_4 to the visible region (**Figure S6a–e**). A similar volcano-type trend as for HER properties is observed from the absorption edges of CN/LDH samples. The E_g values of 2D-C_3N_4 and LDH-3 are estimated as 2.85 and 2.34 eV, respectively, based on the UV-vis DRS spectra (**Figure S6f** and **3c**). Meanwhile, their VB_{XPS} values are determined to be 1.88 and 2.12 eV, respectively. Thus, E_{VB} and E_{CB} can be calculated as +1.79 and −1.06 V for 2D-C_3N_4 and +2.03 and −0.31 V for LDH-3, respectively. The electron work functions (Φ) of 2D-C_3N_4, LDH-3, and CN/LDH-3 are calculated to be 4.25, 5.52, and 4.55 eV, respectively, by using Equation (3),[49] where E_{cutoff} marks the beginning of the secondary photoemission estimated by ultraviolet photoelectron spectra (UPS) analysis in **Figure S7**. The value of the Fermi level (E_F) is the negative value of Φ, and the E_F values for 2D-C_3N_4, LDH-3, and CN/LDH-3 are calculated as −0.60, +0.67, and −0.30 V (*vs*. RHE, pH = 7), respectively, based on the conversion formula (4)[50] and Nernst equation (5)[51]:

$$\Phi = 21.22 - E_{\text{cutoff}} \quad (3)$$

$$E\ (vs.\ \text{RHE, pH} = 0) = -4.44\ \text{V} - E\ (vs.\ \text{vacuum level}) \quad (4)$$

$$E\ (vs.\ \text{RHE, pH} = 7) = E\ (vs.\ \text{RHE, pH} = 0) - 0.059\ \text{pH} \quad (5)$$

The band gap alignment and photocatalytic mechanism are proposed in **Figure 7e** based on the discussion above. Before contact, 2D-C_3N_4 has a smaller work function than LDH-3 with its E_F located above that of LDH-3. Upon the formation of CN/LDH-3 composite, the electrons in 2D-C_3N_4 would spontaneously move to LDH-3 across the interface until their E_F levels match.[52] This creates an internal interfacial electric field from 2D-C_3N_4 to LDH-3, which prevents further electrons transfer from 2D-C_3N_4 to LDH-3. Also, the VB and CB of 2D-C_3N_4 shift down with upward band bending whereas those of LDH-3 shift upward with downward band bending. Under simulated solar illumination, such configuration of band bending at the interface drives the photoexcited electrons in the CB of LDH-3 to the CB of 2D-C_3N_4 for surface HER, while the holes are transferred to the opposite path,[53] forming a type II heterojunction. It was reported that the redox potentials of Ni^{3+}/Ni^{2+} and Fe^{3+}/Fe^{2+} are more positive than those of $TEOA^+$/TEOA, and the accumulated holes in LDH-3 could be readily captured by TEOA, preventing the photo-corrosion of 2D-C_3N_4/NiFe-LDH heterostructure.[54, 55] Owing to the 2D–2D configuration and the strong electronic coupling between 2D-C_3N_4 and LDH-3, the CN/LDH-3 architecture ensures a large external surface area and provides a strong driving force for excellent charge transfer that would lead to fast surface reaction kinetics and improved photocatalytic HER performance.

To validate the charge transfer mechanism, electron spin resonance (ESR) spectra were collected and presented in **Figure S8**. In the dark, no signals of $\bullet O_2^-$ and •OH are observed from any samples. Under simulated sunlight, 2D-C_3N_4 generates only $\bullet O_2^-$ radicals, whereas LDH-3 only generates •OH radicals. This indicates the E_{CB} of 2D-C_3N_4 is more negative than $E(\bullet O_2^-/O_2) = -0.33$ V (*vs*. RHE, pH = 7), and E_{VB} of LDH-3 is more positive than $E(\bullet OH/OH^-)$ = +1.99 V (*vs*. RHE, pH = 7). In the case of CN/LDH-3, much stronger characteristic peaks of

•O_2^- radicals are detected under simulated sunlight. This can be attributed to the accumulation of electrons in the CB of 2D-C_3N_4, which is still more negative than $E(\bullet O_2^-/O_2)$. The •OH signals in CN/LDH-3 are greatly enhanced, even more than those of •O_2^-. It is believed that H_2O_2 is produced and converted to •OH by photo-Fenton reaction with the Fe species in LDH-3 ($Fe^{3+} + H_2O_2 + h\nu \rightarrow Fe^{2+} + HO_2\bullet + H^+$; $Fe^{2+} + H_2O_2 + h\nu \rightarrow Fe^{3+} + \bullet OH + OH^-$).[56] Both 2D-$C_3N_4$ and LDH-3 can produce H_2O_2 due to their CB bands located more negative than $E(O_2/H_2O_2)$ = +0.28 V (*vs*. RHE, pH = 7). The E_{VB} of LDH-3 is slightly more positive (0.04 V) than $E(\bullet OH/OH^-)$, thus part of the •OH signal in LDH-3 may be originated from the photo-Fenton reaction (**Figure 7e**, left panel). Such a transformation of H_2O_2 to •OH is not possible in 2D-C_3N_4 without Fe species. These ESR results are consistent with the CB and VB potentials determined in **Figure 7e**, confirming the construction of a type II structure.

4. CONCLUSIONS

In summary, 2D-C_3N_4 was coupled with morphology-controlled NiFe-LDH nanoflowers to successfully form a type II heterostructure photocatalyst by interface engineering. The structure and morphology of LDH were tuned using NH_4F as a structure-directing agent, which enables a fine interfacial tuning *via* coupling with 2D-C_3N_4. The as-prepared CN/LDH-3 composite exhibits excellent photocatalytic HER performance under simulated sunlight with an optimum H_2 production rate of 3,087 μmol g^{-1} h^{-1} (6,817 μmol g^{-1} h^{-1} with 3 wt.% Pt), which is almost 14 times higher than that of 2D-C_3N_4. Such superior performance is ascribed mainly to the synergistic effect and the suitable band gap alignment between 2D-C_3N_4 and LDH-3. With higher specific area and efficient interfacial charge transfer, the formation of 2D-C_3N_4/LDH interface can effectively prolong the lifetime of electron–hole pairs with excellent stability against photo-corrosion. This work demonstrates an effective strategy to employ earth-abundant elements-based LDH as a co-catalyst to construct a type II heterojunction to improve photocatalytic H_2 evolution.

ASSOCIATED CONTENT

Supporting Information

Supporting Information is available from the ACS Publications website or from the author. Digital photos of products, N_2 adsorption–desorption isotherms, UV–vis spectra, UPS spectra, ESR spectra, zeta potentials, fitted parameters for EIS analysis, and lifetimes of photogenerated charge carriers.

AUTHOR INFORMATION

Corresponding Author

* Lawrence Yoon Suk Lee: lawrence.ys.lee@polyu.edu.hk

Author Contributions

J. Y. and X. Z. contributed equally to this work.

Notes

All authors have given approval to the final version of the manuscript and declare no competing financial interest.

ACKNOWLEDGMENTS

We gratefully acknowledge the financial supports from the Innovation and Technology Commission of Hong Kong and The Hong Kong Polytechnic University (1-BE0Y). J. Y. acknowledges the Postdoctoral Fellowships Scheme from the Hong Kong Polytechnic University (1-YW3J) and Natural Science Foundation of Jiangsu Province (BK20180887).

Received: ((will be filled in by the editorial staff))

Revised: ((will be filled in by the editorial staff))

Published online: ((will be filled in by the editorial staff))

REFERENCES

1. Dai, B.; Fang, J.; Yu, Y.; Sun, M.; Huang, H.; Lu, C.; Kou, J.; Zhao, Y.; Xu, Z., Construction of Infrared-Light-Responsive Photoinduced Carriers Driver for Enhanced Photocatalytic Hydrogen Evolution. *Adv. Mater.* **2020**, *32*, 1906361.
2. Zhang, G.; Li, G.; Heil, T.; Zafeiratos, S.; Lai, F.; Savateev, A.; Antonietti, M.; Wang, X., Tailoring the Grain Boundary Chemistry of Polymeric Carbon Nitride for Enhanced Solar Hydrogen Production and CO_2 Reduction. *Angew. Chem. Int. Ed.* **2019**, *58*, 3433-3437.
3. Yan, B.; Du, C.; Yang, G. W., Constructing Built-in Electric Field in Ultrathin Graphitic Carbon Nitride Nanosheets by N and O Codoping for Enhanced Photocatalytic Hydrogen Evolution Activity. *Small* **2020**, *16*, 1905700.
4. Wang, S.; He, F.; Zhao, X.; Zhang, J.; Ao, Z.; Wu, H.; Yin, Y.; Shi, L.; Xu, X.; Zhao, C.; Wang, S.; Sun, H., Phosphorous Doped Carbon Nitride Nanobelts for Photodegradation of Emerging Contaminants and Hydrogen Evolution. *Appl. Catal., B* **2019**, *257*, 117931.
5. Li, J.; Yang, W.; Wu, A.; Zhang, X.; Xu, T.; Liu, B., Band-Gap Tunable 2D Hexagonal $(GaN)_{1-x}(ZnO)_x$ Solid-Solution Nanosheets for Photocatalytic Water Splitting. *ACS Appl. Mater. Interfaces* **2020**, *12*, 8583-8591.
6. Yuan, Y.-J.; Chen, D.-Q.; Xiong, M.; Zhong, J.-S.; Wan, Z.-Y.; Zhou, Y.; Liu, S.; Yu, Z.-T.; Yang, L.-X.; Zou, Z.-G., Bandgap Engineering of $(AgIn)_xZn_{2(1-x)}S_2$ Quantum Dot Photosensitizers for Photocatalytic H_2 Generation. *Appl. Catal., B* **2017**, *204*, 58-66.
7. Acharya, L.; Nayak, S.; Pattnaik, S. P.; Acharya, R.; Parida, K., Resurrection of Boron Nitride in p-n Type-II Boron Nitride/B-doped-g-C_3N_4 Nanocomposite During Solid-State Z-Scheme Charge Transfer Path for the Degradation of Tetracycline Hydrochloride. *J. Colloid Interface Sci.* **2020**, *566*, 211-223.
8. Zhang, J.; Zhang, G.; Chen, X.; Lin, S.; Mohlmann, L.; Dolega, G.; Lipner, G.; Antonietti, M.; Blechert, S.; Wang, X., Co-Monomer Control of Carbon Nitride Semiconductors to

Optimize Hydrogen Evolution with Visible Light. *Angew. Chem. Int. Ed. Engl.* **2012**, *51*, 3183-3187.

9. Niu, P.; Zhang, L.; Liu, G.; Cheng, H.-M., Graphene-Like Carbon Nitride Nanosheets for Improved Photocatalytic Activities. *Adv. Funct. Mater.* **2012**, *22*, 4763-4770.
10. Yang, S. B.; Gong, Y. J.; Zhang, J. S.; Zhan, L.; Ma, L. L.; Fang, Z. Y.; Vajtai, R.; Wang, X. C.; Ajayan, P. M., Exfoliated Graphitic Carbon Nitride Nanosheets as Efficient Catalysts for Hydrogen Evolution under Visible Light. *Adv. Mater.* **2013**, *25*, 2452-2456.
11. Wang, Y.; Du, P.; Pan, H.; Fu, L.; Zhang, Y.; Chen, J.; Du, Y.; Tang, N.; Liu, G., Increasing Solar Absorption of Atomically Thin 2D Carbon Nitride Sheets for Enhanced Visible-Light Photocatalysis. *Adv. Mater.* **2019**, *31*, 1807540.
12. Zhang, J.; Li, Y.; Zhao, X.; Zhang, H.; Wang, L.; Chen, H.; Wang, S.; Xu, X.; Shi, L.; Zhang, L.-C.; Veder, J.-P.; Zhao, S.; Nealon, G.; Wu, M.; Wang S.; Sun H., A Hydrogen-Initiated Chemical Epitaxial Growth Strategy for In-Plane Heterostructured Photocatalyst. *ACS Nano* **2020**, *14*, 17505-17514.
13. Bhunia, K.; Chandra, M.; Khilari, S.; Pradhan, D., Bimetallic PtAu Alloy Nanoparticles-Integrated g-C_3N_4 Hybrid as an Efficient Photocatalyst for Water-to-Hydrogen Conversion. *ACS Appl. Mater. Interfaces* **2018**, *11*, 478-488.
14. Ma, R.; Zhang, S.; Li, L.; Gu, P.; Wen, T.; Khan, A.; Li, S.; Li, B.; Wang, S.; Wang, X., Enhanced Visible-Light-Induced Photoactivity of Type-II CeO_2/g-C_3N_4 Nanosheet toward Organic Pollutants Degradation. *ACS Sustainable Chem. Eng.* **2019**, *7*, 9699-9708.
15. Kim, W. J.; Jang, E.; Park, T. J., Enhanced Visible-Light Photocatalytic Activity of ZnS/g-C_3N_4 Type-II Heterojunction Nanocomposites Synthesized with Atomic Layer Deposition. *Appl. Surf. Sci.* **2017**, *419*, 159.
16. Wang, Q.; O'Hare, D., Recent Advances in the Synthesis and Application of Layered Double Hydroxide (LDH) Nanosheets. *Chem. Rev.* **2012**, *112*, 4124-4155.

17. Zheng, Y.; Cheng, B.; You, W.; Yu, J.; Ho, W., 3D Hierarchical Graphene Oxide-NiFe LDH Composite with Enhanced Adsorption Affinity to Congo Red, Methyl Orange and Cr(VI) Ions. *J. Hazard. Mater.* **2019**, *369*, 214-225.

18. Nayak, S.; Parida, K., Superactive NiFe-LDH/Graphene Nanocomposites as Competent Catalysts for Water Splitting Reactions. *Inorg. Chem. Front.* **2020**, *7*, 3805-3836.

19. Boppella, R.; Choi, C. H.; Moon, J.; Ha Kim, D., Spatial Charge Separation on Strongly Coupled 2D-Hybrid of rGO/$La_2Ti_2O_7$/NiFe-LDH Heterostructures for Highly Efficient Noble Metal Free Photocatalytic Hydrogen Generation. *Appl. Catal., B* **2018**, *239*, 178-186.

20. Zhong, H.; Liu, T.; Zhang, S.; Li, D.; Tang, P.; Alonso-Vante, N.; Feng, Y., Template-Free Synthesis of Three-Dimensional NiFe-LDH Hollow Microsphere with Enhanced OER Performance in Alkaline Media. *J. Energy Chem.* **2019**, *33*, 130-137.

21. She, X.; Wu, J.; Zhong, J.; Xu, H.; Yang, Y.; Vajtai, R.; Lou, J.; Liu, Y.; Du, D.; Li, H.; Ajayan, P. M., Oxygenated Monolayer Carbon Nitride for Excellent Photocatalytic Hydrogen Evolution and External Quantum Efficiency. *Nano Energy* **2016**, *27*, 138-146.

22. Xu, H.; Wang, B.; Shan, C.; Xi, P.; Liu, W.; Tang, Y., Ce-Doped NiFe-Layered Double Hydroxide Ultrathin Nanosheets/Nanocarbon Hierarchical Nanocomposite as an Efficient Oxygen Evolution Catalyst. *ACS Appl. Mater. Interfaces* **2018**, *10*, 6336-6345.

23. Li, X.; Wang, N.; Huang, Z.; Zhang, L.; Xie, Y.-B.; An, Q.-F.; Ji, S., A Vertically Channeled Lamellar Membrane for Molecular Sieving of Water from Organic Solvents. *J. Mater. Chem. A* **2018**, *6*, 18095-18102.

24. Chen, Q. Q.; Hou, C. C.; Wang, C. J.; Yang, X.; Shi, R.; Chen, Y., Ir^{4+}-Doped NiFe LDH to Expedite Hydrogen Evolution Kinetics as a Pt-Like Electrocatalyst for Water Splitting. *Chem. Commun. (Camb.)* **2018**, *54*, 6400-6403.

25. Stoyl P. Stoylov, M. V. S., Molecular and Colloidal Electro-Optics. *CRC Press Inc.* **2006**, 134, 594.

26. Nayak, S.; Swain, G.; Parida, K., Enhanced Photocatalytic Activities of Rhb Degradation and H_2 Evolution from in Situ Formation of the Electrostatic Heterostructure MoS_2/NiFe LDH Nanocomposite through the Z-Scheme Mechanism via P-N Heterojunctions. *ACS Appl. Mater. Interfaces* **2019**, *11*, 20923-20942.

27. Ma, J.; Ding, J.; Yu, L.; Li, L.; Kong, Y.; Komarneni, S., Biocl Dispersed on NiFe-LDH Leads to Enhanced Photo-Degradation of Rhodamine B Dye. *Appl. Clay Sci.* **2015**, *109-110*, 76-82.

28. Mei, L.; Liao, L.; Wang, Z.; Xu, C., Interactions between Phosphoric/Tannic Acid and Different Forms of FeOOH. *Adv. Mater. Sci. Eng.* **2015**, *2015*, 1-10.

29. Weckler, B.; Lutz, H. D., Lattice Vibration Spectra. Part XCV. Infrared Spectroscopic Studies on the Iron Oxide Hydroxides Goethite (α), Akaganéite (β), Lepidocrocite (γ), and Feroxyhite (δ). *Eur. J. Solid State Inorg. Chem.* **1998**, *35*, 531-544.

30. Ma, Y.; Wang, Y.; Xie, D.; Gu, Y.; Zhang, H.; Wang, G.; Zhang, Y.; Zhao, H.; Wong, P. K., NiFe-Layered Double Hydroxide Nanosheet Arrays Supported on Carbon Cloth for Highly Sensitive Detection of Nitrite. *ACS Appl. Mater. Interfaces* **2018**, *10*, 6541-6551.

31. Yu, L.; Zhou, H.; Sun, J.; Qin, F.; Yu, F.; Bao, J.; Yu, Y.; Chen, S.; Ren, Z., Cu Nanowires Shelled with NiFe Layered Double Hydroxide Nanosheets as Bifunctional Electrocatalysts for Overall Water Splitting. *Energy Environ. Sci.* **2017**, *10*, 1820-1827.

32. Wang, Y.; Jiang, C.; Le, Y.; Cheng, B.; Yu, J., Hierarchical Honeycomb-Like Pt/NiFe-LDH/rGO Nanocomposite with Excellent Formaldehyde Decomposition Activity. *Chem. Eng. J.* **2019**, *365*, 378-388.

33. Guo, W.; Li, D.; Zhong, D.; Chen, S.; Hao, G.; Liu, G.; Li, J.; Zhao, Q., Loading FeOOH on $Ni(OH)_2$ Hollow Nanorods to Obtain a Three-Dimensional Sandwich Catalyst with Strong Electron Interactions for an Efficient Oxygen Evolution Reaction. *Nanoscale* **2020**, *12*, 983-990.

34. Zhao, Y.; Jia, X.; Waterhouse, G. I. N.; Wu, L.-Z.; Tung, C.-H.; O'Hare, D.; Zhang, T., Layered Double Hydroxide Nanostructured Photocatalysts for Renewable Energy Production. *Adv. Energy Mater.* **2016**, *6*, 1501974.

35. Yu, H.; Shi, R.; Zhao, Y.; Bian, T.; Zhao, Y.; Zhou, C.; Waterhouse, G. I. N.; Wu, L. Z.; Tung, C. H.; Zhang, T., Alkali-Assisted Synthesis of Nitrogen Deficient Graphitic Carbon Nitride with Tunable Band Structures for Efficient Visible-Light-Driven Hydrogen Evolution. *Adv. Mater.* **2017**, *29*, 1605148.

36. Jiang, J.; Liu, J. P.; Huang, X. T.; Li, Y. Y.; Ding, R. M.; Ji, X. X.; Hu, Y. Y.; Chi, Q. B.; Zhu, Z. H., General Synthesis of Large-Scale Arrays of One-Dimensional Nanostructured Co_3O_4 Directly on Heterogeneous Substrates. *Cryst. Growth Des.* **2010**, *10*, 70-75.

37. Chen, Y.; Qu, B.; Hu, L.; Xu, Z.; Li, Q.; Wang, T., High-Performance Supercapacitor and Lithium-Ion Battery Based on 3D Hierarchical NH_4F-Induced Nickel Cobaltate Nanosheet-Nanowire Cluster Arrays as Self-Supported Electrodes. *Nanoscale* **2013**, *5*, 9812-9820.

38. Zhang, G.; Lan, Z.-A.; Lin, L.; Lin, S.; Wang, X., Overall Water Splitting by Pt/g-C_3N_4 Photocatalysts without Using Sacrificial Agents. *Chem. Sci.* **2016**, *7*, 3062-3066.

39. Xu, Q.; Cheng, B.; Yu, J.; Liu, G., Making Co-Condensed Amorphous Carbon/g-C_3N_4 Composites with Improved Visible-Light Photocatalytic H_2-Production Performance Using Pt as Cocatalyst. *Carbon* **2017**, *118*, 241-249.

40. Xu, Y.; Ge, F.; Chen, Z.; Huang, S.; Wei, W.; Xie, M.; Xu, H.; Li, H., One-Step Synthesis of Fe-Doped Surface-Alkalinized g-C_3N_4 and Their Improved Visible-Light Photocatalytic Performance. *Appl. Surf. Sci.* **2019**, *469*, 739-746.

41. Jiang, J.; Ou-yang, L.; Zhu, L.; Zheng, A.; Zou, J.; Yi, X.; Tang, H., Dependence of Electronic Structure of g-C_3N_4 on the Layer Number of Its Nanosheets: A Study by Raman Spectroscopy Coupled with First-Principles Calculations. *Carbon* **2014**, *80*, 213-221.

42. Zhang, G.; Zhang, J.; Zhang, M.; Wang, X., Polycondensation of Thiourea into Carbon Nitride Semiconductors as Visible Light Photocatalysts. *J. Mater. Chem.* **2012**, *22*, 8083-8091.

43. Barsoukov, E.; Macdonald, J. R., Impedance Spectroscopy Theory, Experiment, and Applications, *John Wiley & Sons* **2005**, 13-20.

44. Zheng, W.; Li, Y.; Lee, L. Y. S., Insights into the Transition Metal Ion-Mediated Electrooxidation of Glucose in Alkaline Electrolyte. *Electrochim. Acta* **2019**, *308*, 9-19.

45. Jiang, Z.; Wang, B.; Li, Y.; Chan, H. S.; Sun, H.; Wang, T.; Li, H.; Yuan, S.; Leung, M. K. H.; Lu, A.; Wong, P. K., Solar-Light-Driven Rapid Water Disinfection by Ultrathin Magnesium Titanate/Carbon Nitride Hybrid Photocatalyst: Band Structure Analysis and Role of Reactive Oxygen Species. *Appl. Catal., B* **2019**, *257*, 117898.

46. Cao, F.; Meng, L.; Wang, M.; Tian, W.; Li, L., Gradient Energy Band Driven High-Performance Self-Powered Perovskite/Cds Photodetector. *Adv. Mater.* **2019**, *31*, 1806725.

47. Xia, P. F.; Cao, S. W.; Zhu, B. C.; Liu, M. J.; Shi, M. S.; Yu, J. G.; Zhang, Y. F., Designing a 0D/2D S-Scheme Heterojunction over Polymeric Carbon Nitride for Visible-Light Photocatalytic Inactivation of Bacteria. *Angew. Chem. Int. Ed.* **2020**, *59*, 5218-5225.

48. Nayak, S.; Mohapatra, L.; Parida, K., Visible Light-Driven Novel g-C_3N_4/NiFe-LDH Composite Photocatalyst with Enhanced Photocatalytic Activity Towards Water Oxidation and Reduction Reaction. *J. Mater. Chem. A* **2015**, *3*, 18622-18635.

49. Zhang, J.; Bai, D.; Jin, Z.; Bian, H.; Wang, K.; Sun, J.; Wang, Q.; Liu, S., 3D-2D-0D Interface Profiling for Record Efficiency All-Inorganic $CsPbBrI_2$ Perovskite Solar Cells with Superior Stability. *Adv. Energy Mater.* **2018**, *8*, 1703246.

50. Liu, J.; Liu, Y.; Liu, N. Y.; Han, Y. Z.; Zhang, X.; Huang, H.; Lifshitz, Y.; Lee, S. T.; Zhong, J.; Kang, Z. H., Metal-Free Efficient Photocatalyst for Stable Visible Water Splitting via a Two-Electron Pathway. *Science* **2015**, *347*, 970-974.

51. Cao, S.; Shen, B.; Tong, T.; Fu, J.; Yu, J., 2D/2D Heterojunction of Ultrathin MXene/Bi_2WO_6 Nanosheets for Improved Photocatalytic CO_2 Reduction. *Adv. Funct. Mater.* **2018**, *28*, 1800136.

52. Zhang, Z.; Yates, J. T., Band Bending in Semiconductors: Chemical and Physical Consequences at Surfaces and Interfaces. *Chem. Rev.* **2012**, *112*, 5520-5551.

53. Huang, Z.-F.; Song, J.; Wang, X.; Pan, L.; Li, K.; Zhang, X.; Wang, L.; Zou, J.-J., Switching Charge Transfer of $C_3N_4/W_{18}O_{49}$ from Type-II to Z-Scheme by Interfacial Band Bending for Highly Efficient Photocatalytic Hydrogen Evolution. *Nano Energy* **2017**, *40*, 308-316.

54. Qin, Z.; Chen, Y.; Huang, Z.; Su, J.; Guo, L., A Bifunctional NiCoP-Based Core/Shell Cocatalyst to Promote Separate Photocatalytic Hydrogen and Oxygen Generation over Graphitic Carbon Nitride. *J. Mater. Chem. A* **2017**, *5*, 19025-19035.

55. Chen, X.; Zhang, J.; Fu, X.; Antonietti, M.; Wang, X., Fe-g-C_3N_4-Catalyzed Oxidation of Benzene to Phenol Using Hydrogen Peroxide and Visible Light. *J. Am. Chem. Soc.* **2009**, *131*, 11658-11659.

56. Nawaz, M.; Shahzad, A.; Tahir, K.; Kim, J.; Moztahida, M.; Jang, J.; Alam, M. B.; Lee, S.-H.; Jung, H.-Y.; Lee, D. S., Photo-Fenton Reaction for the Degradation of Sulfamethoxazole Using a Multi-Walled Carbon Nanotube-$NiFe_2O_4$ Composite. *Chem. Eng. J.* **2020**, *382*, 123053.

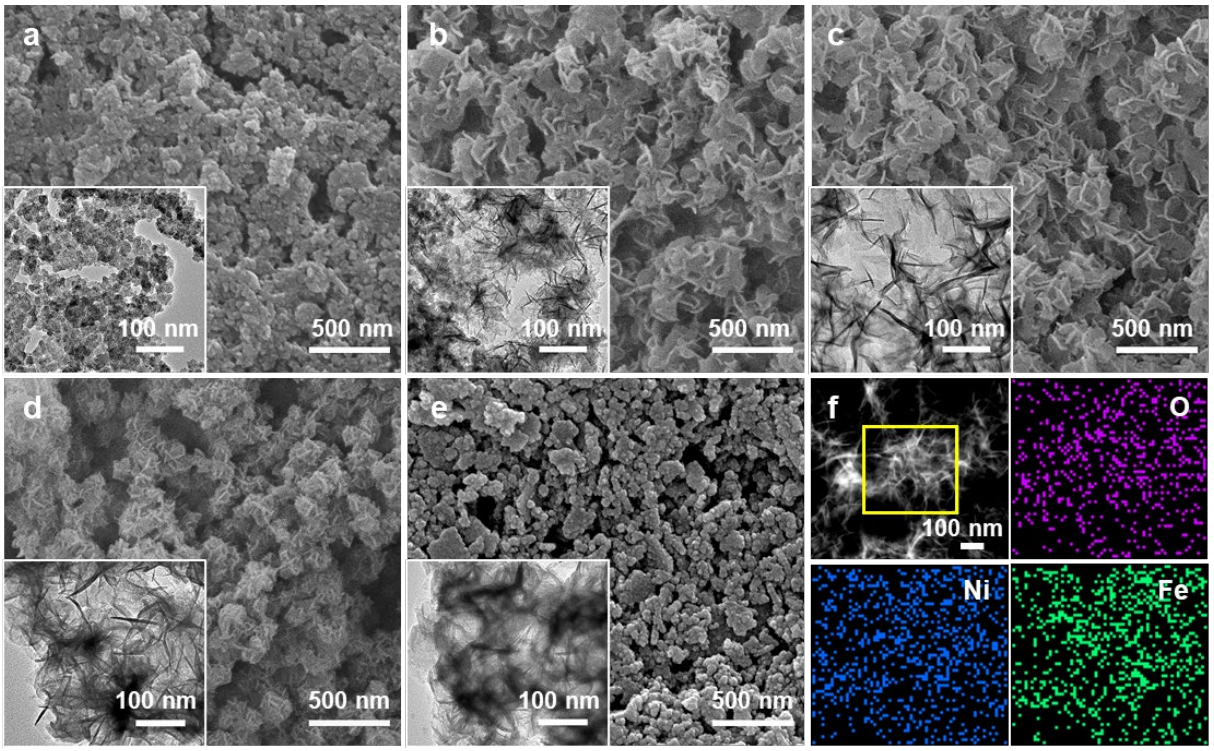

Figure 1. SEM images of (a) LDH-1, (b) LDH-2, (c) LDH-3, (d) LDH-4, and (e) LDH-5. Insets are the corresponding TEM images. (f) Elemental mapping images of LDH-3.

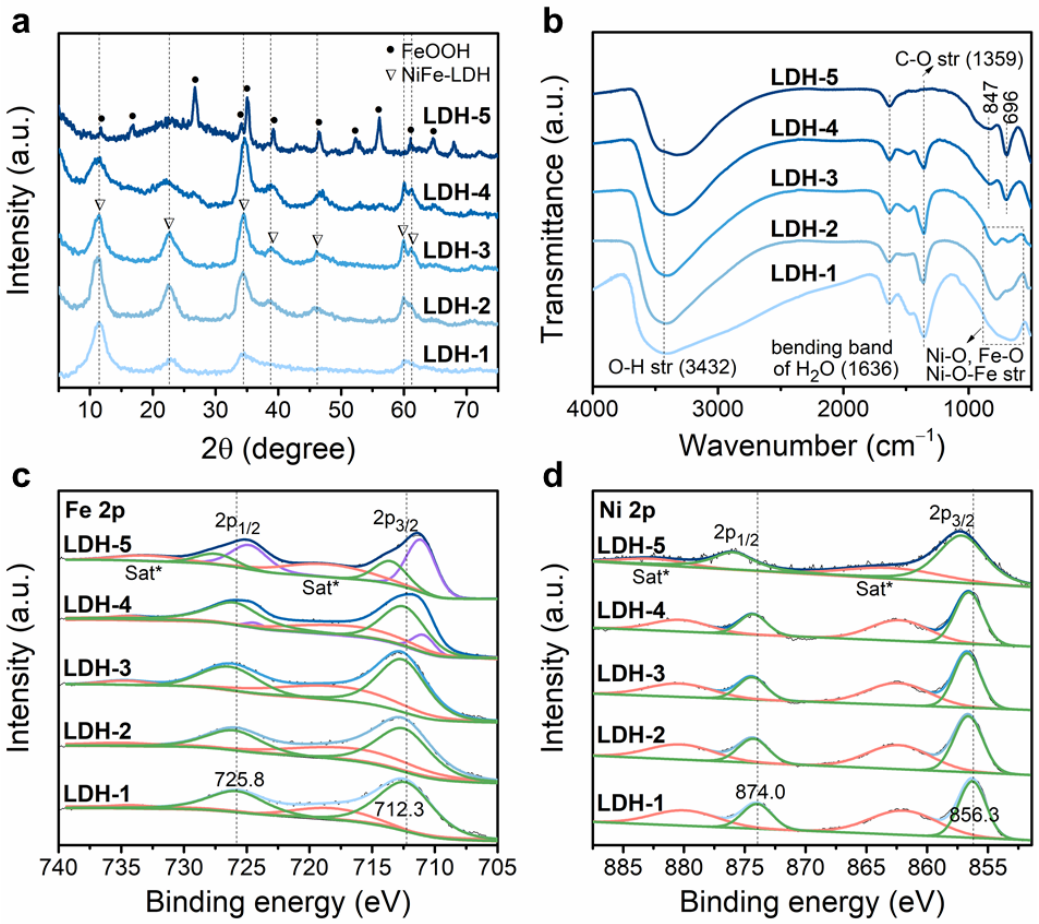

Figure 2. (a) XRD spectra, (b) FT-IR spectra, and high-resolution XPS spectra in (c) Fe 2p and (d) Ni 2p regions of LDH samples.

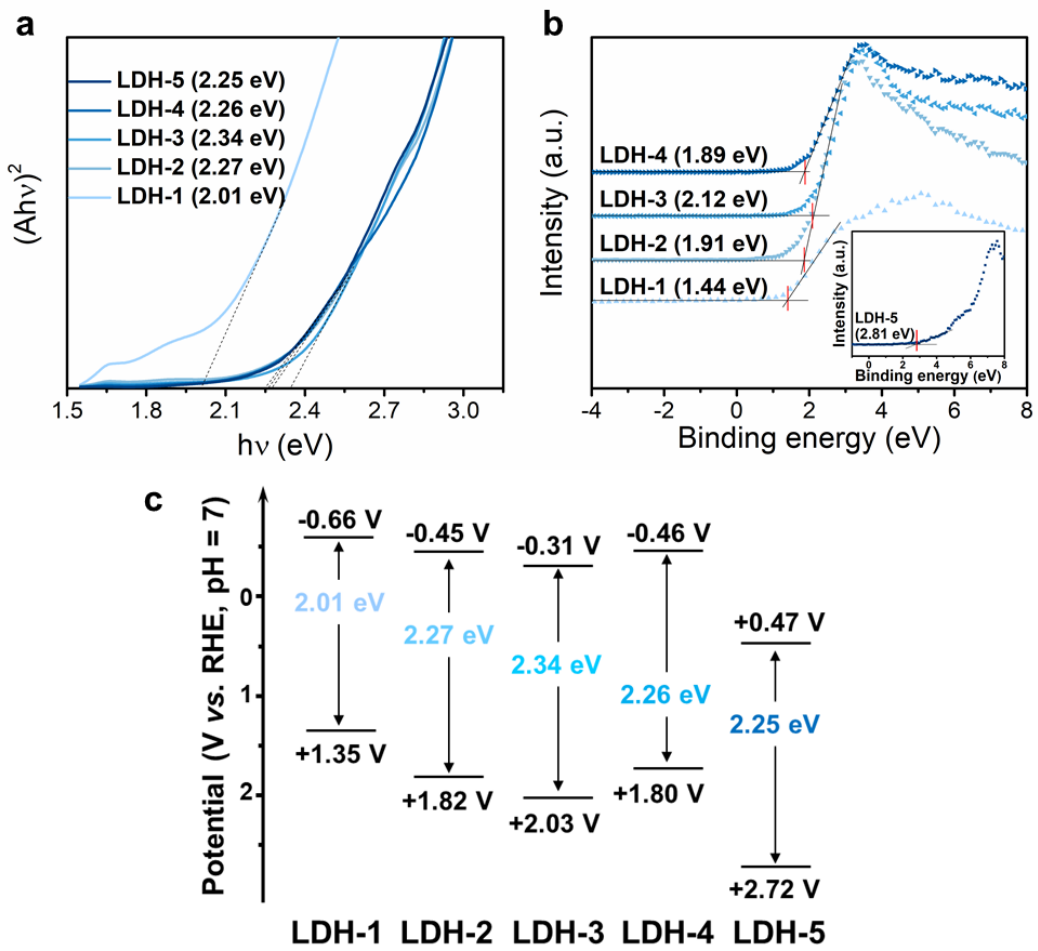

Figure 3. (a) UV-vis absorption spectra with estimated band gap energies, (b) VB_{XPS} spectra, and (c) the proposed band structures of LDH samples.

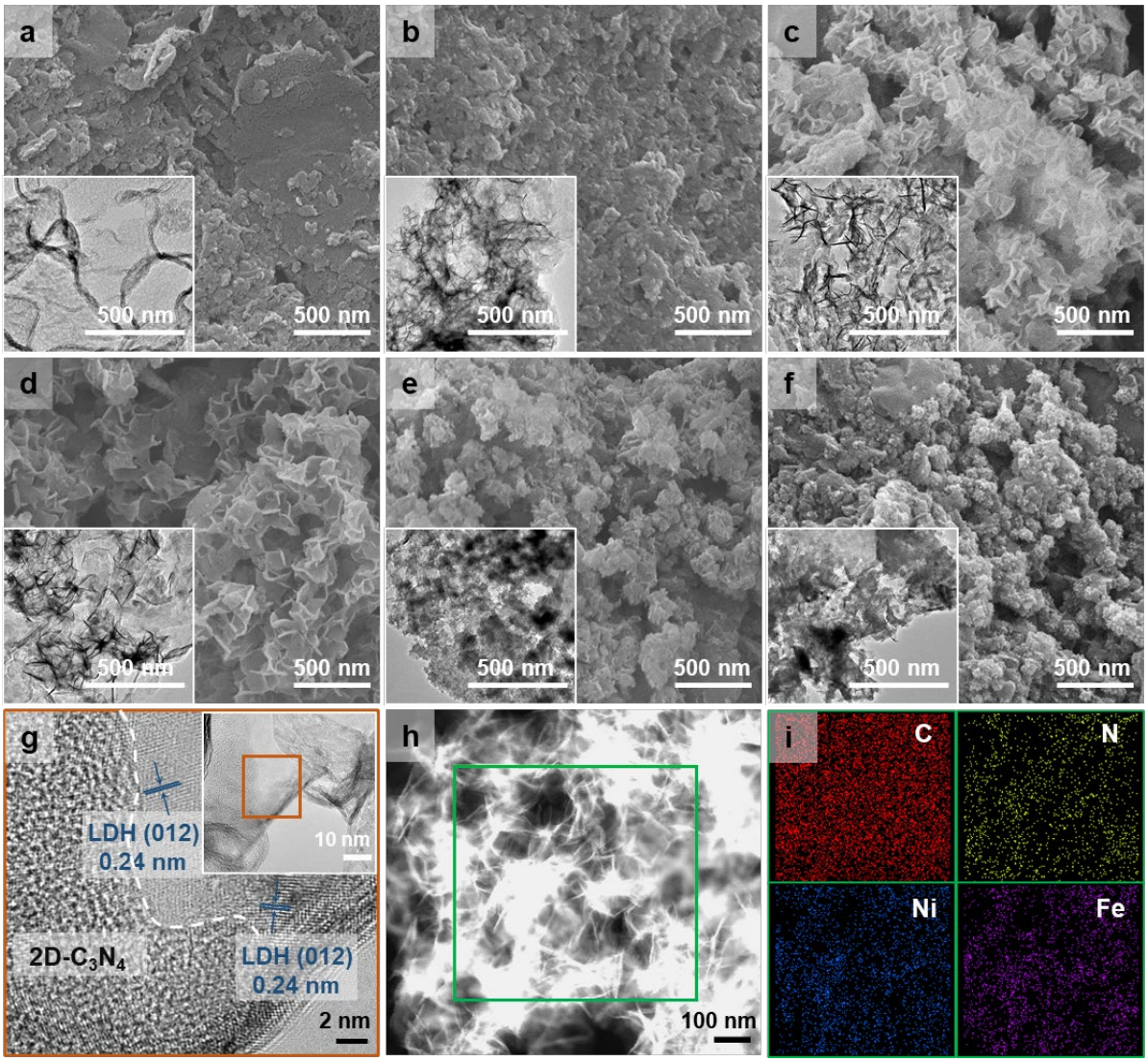

Figure 4. SEM images of (a) 2D-C_3N_4, (b) CN/LDH-1, (c) CN/LDH-2, (d) CN/LDH-3, (e) CN/LDH-4, and (f) CN/LDH-5. Insets are the corresponding TEM images. (g) HRTEM and (h, i) EDX elemental mapping images of CN/LDH-3.

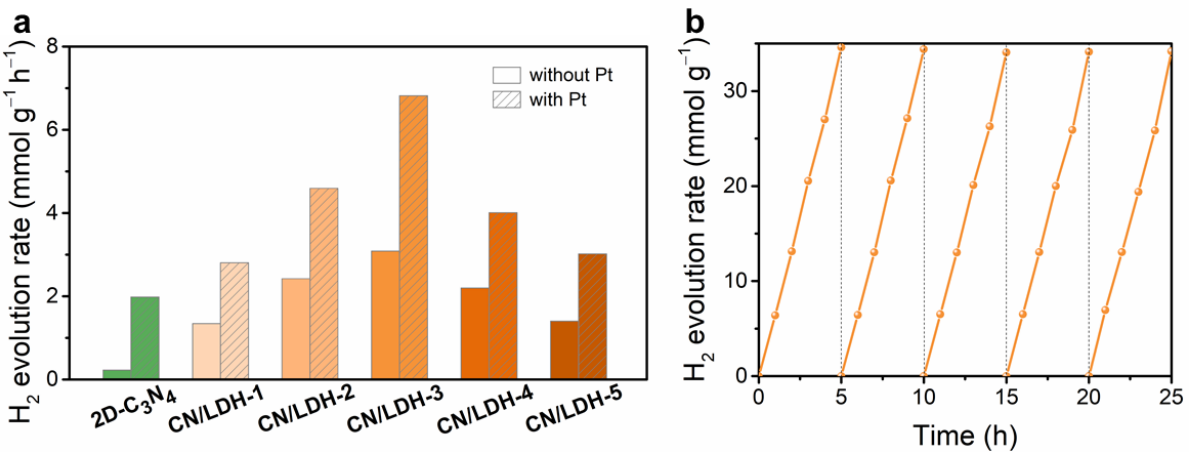

Figure 5. (a) Photocatalytic H_2 evolution over 2D-C_3N_4 and CN/LDH samples. (b) Long-term photocatalytic H_2 evolution rate of CN/LDH-3.

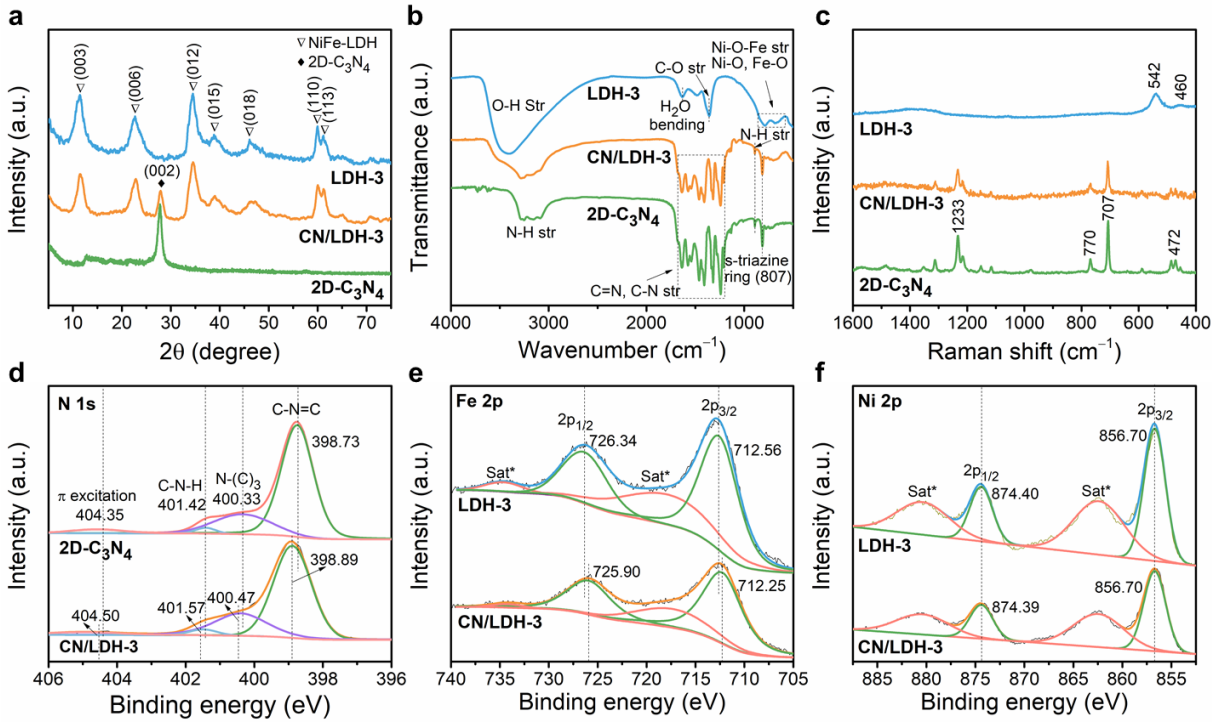

Figure 6. (a) XRD, (b) FT-IR, (c) Raman spectra, and high-resolution XPS spectra in (d) N 1s, (e) Fe 2p, and (f) Ni 2p regions of 2D-C_3N_4, LDH-3, and CN/LDH-3.

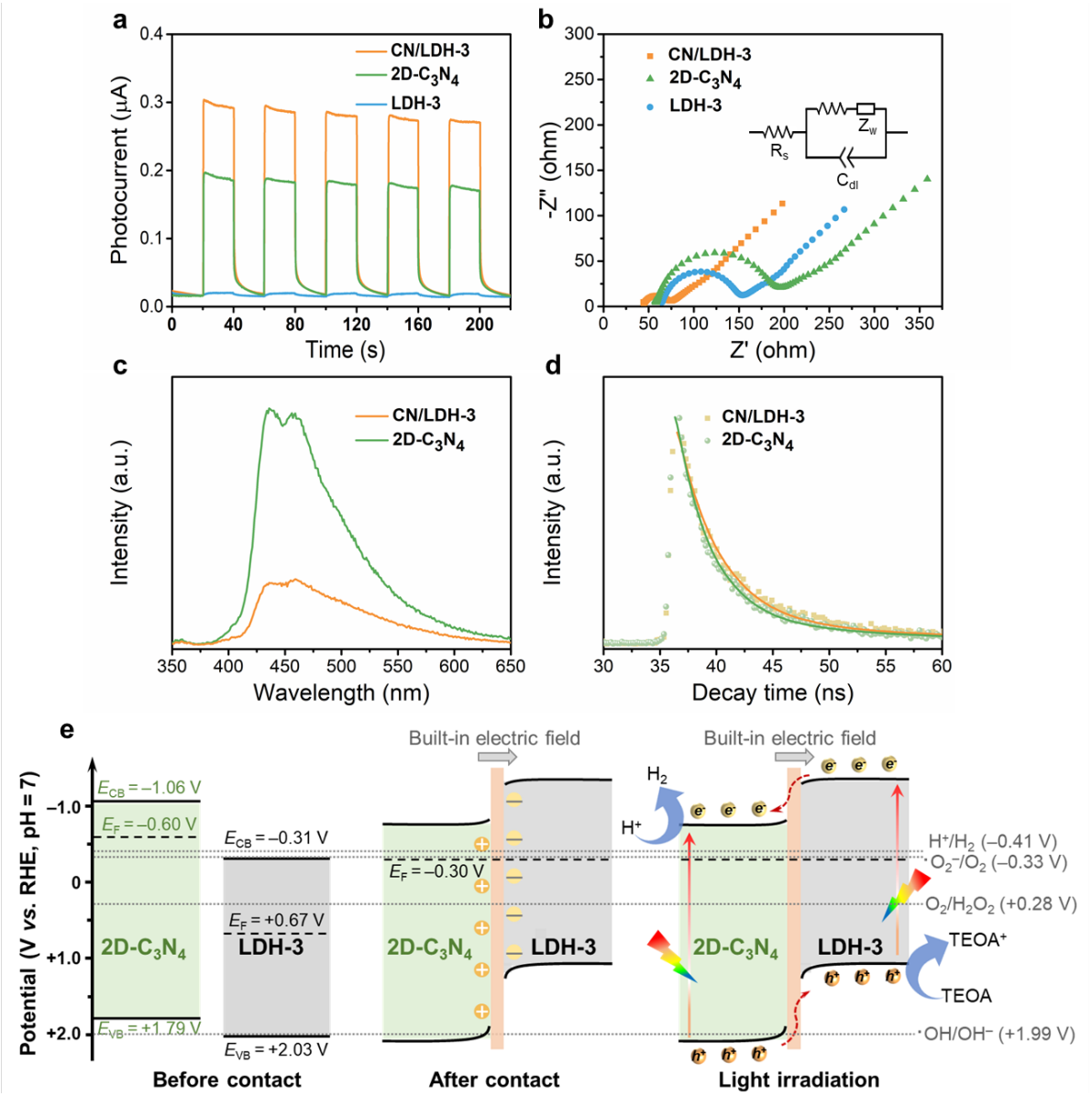

Figure 7. (a) Photocurrent responses at 0 V under chopped light illumination and (b) EIS spectra measured at OCP of 2D-C_3N_4, LDH-3, and CN/LDH-3. Inset is the equivalent circuit. (c) PL and (d) TRPL spectra at 325 nm obtained from 2D-C_3N_4 and CN/LDH-3. (e) Proposed mechanism for the enhanced H_2 evolution under light irradiation.

Table of contents

Interface Engineering of 2D-C_3N_4/NiFe-LDH Heterostructure for Highly Efficient Photocatalytic Hydrogen Evolution